Time-Dependent Cation Selectivity of Titanium Carbide MXene in Aqueous Solution

Lei Wang, Mohammad Torkamanzadeh, Ahmad Majed, Yuan Zhang, Qingsong Wang, Ben Breitung, Guang Feng, Michael Naguib, and Volker Presser*

Electrochemical ion separation is a promising technology to recover valuable ionic species from water. Pseudocapacitive materials, especially 2D materials, are up-and-coming electrodes for electrochemical ion separation. For implementation, it is essential to understand the interplay of the intrinsic preference of a specific ion (by charge/size), kinetic ion preference (by mobility), and crystal structure changes. $Ti_3C_2T_z$ MXene is chosen here to investigate its selective behavior toward alkali and alkaline earth cations. Utilizing an online inductively coupled plasma system, it is found that $Ti_3C_2T_z$ shows a time-dependent selectivity feature. In the early stage of charging (up to about 50 min), K^+ is preferred, while ultimately Ca^{2+} and Mg^{2+} uptake dominate; this unique phenomenon is related to dehydration energy barriers and the ion exchange effect between divalent and monovalent cations. Given the wide variety of MXenes, this work opens the door to a new avenue where selective ion-separation with MXene can be further engineered and optimized.

1. Introduction

Ion separation is an essential process to extract valuable metal from natural water[1] and achieve sustainable development.[2] Most commonly, ion separation is studied through adsorption[3] or membrane-based sieving processes[4] and is extended to organic compounds.[5] In addition to seeking reduced cost and energy consumption approaches, there is also a strong motivation to explore and implement more sustainable ion separation technologies.[6] Recently, electrochemical ion separation

has emerged as a promising alternative to traditional separation processes due to its high selectivity metrics and energy efficiency.[7]

Depending on the nature of electroactive material, the ion immobilization and separation process mechanisms are different. For example, nanoporous carbons immobilize ions via electrosorption. Sub-nanometer pores may cause ion sieving or require ions to (partially) shed their solvation shell; this effect enables further tunability of the ion selectivity.[8] Even more confined sites for ion uptake are found in Faradaic materials.[9] Thereby, processes such as ion intercalation or other redox processes enable selectivity toward certain cations or anions.[9,10] For example, $LiMn_2O_4$ provides facile intercalation into its crystal structure only for specific ions with matched size and valence, aligning with intrinsic ion selectivity.[11] Other materials like TiS_2[12] show potential-dependent (tunable) ion selectivity according to the hydration energy of ions. This mechanism is linked with the specific onset potential for ion intercalation (or other redox processes), which gives rise to the unique battery-like feature in electrochemical measurements.[13] Yet, the ion selectivity of pseudocapacitive materials has remained largely unexplored.[14]

MXene is a promising, quickly growing, and novel family of 2D metal carbides or nitrates.[15] The ability to reversibly

L. Wang, M. Torkamanzadeh, Y. Zhang, Q. Wang, V. Presser
INM – Leibniz Institute for New Materials
D2 2, 66123 Saarbrücken, Germany
E-mail: volker.presser@leibniz-inm.de

L. Wang, M. Torkamanzadeh, Y. Zhang, V. Presser
Department of Materials Science and Engineering
Saarland University
Campus D2 2, 66123 Saarbrücken, Germany

A. Majed, M. Naguib
Department of Physics and Engineering Physics
Tulane University
New Orleans, LA 70118, USA

Q. Wang, B. Breitung
Institute of Nanotechnology
Karlsruhe Institute of Technology
Hermann-von-Helmholtz-Platz 1, 76344 Eggenstein-Leopoldshafen, Germany

G. Feng
State Key Laboratory of Coal Combustion
School of Energy and Power Engineering
Huazhong University of Science and Technology
Wuhan, Hubei 430074, China

G. Feng
Nano Interface Centre for Energy
School of Energy and Power Engineering
HUST
Wuhan, Hubei 430074, China

V. Presser
Saarene
Saarland Center for Energy Materials and Sustainability
Campus C4 2, 66123 Saarbrücken, Germany

The ORCID identification number(s) for the author(s) of this article can be found under https://doi.org/10.1002/adsu.202100383.

**ADVANCED
SCIENCE NEWS**

www.advancedsciencenews.com

**ADVANCED
SUSTAINABLE
SYSTEMS**

www.advsustainsys.com

intercalate cations and anions between the MXene-layers[16] yields a pseudocapacitive response, while the carbide/nitride core provides rapid charge transport.[17] Moreover, the surface functional groups such as −F, −OH, and −O on the transition metal atoms formed during the etching process facilitate easier cation intercalation.[18] Thereby, MXenes are widely studied in electrochemical energy storage,[19] water purification,[20] and sensing,[21] among other applications. Regarding aqueous media, Gao et al. used computational simulations to study the positionings of the cations within the MXene slit pores and found that Li^+, Na^+, and K^+ display specific adsorption on the pore surface while Cs^+ and Mg^{2+} are located in the pore center.[22] Recently, Sun et al. reported that titanium carbide-based MXene showed selectivity toward Ca^{2+} compared with Na^+ and Mg^{2+}.[23] The latter work limited its scope to three cations (Ca^{2+}, Mg^{2+}, and Na^+) and the influence of the anode on the selectivity performance of the MXene cathode.

Our work investigates the intercalation process of $Ti_3C_2T_z$ in a multi-cation aqueous electrolyte and the competition for intrinsic and time-dependent preferences between different cations. Using online chemical monitoring with inductively coupled plasma optical emission spectroscopy (ICP-OES), we find that the $Ti_3C_2T_z$ exhibits a time-dependent selectivity between Li^+, Na^+, K^+, Ca^{2+}, and Mg^{2+}. At the same time, there is an ion-exchange phenomenon between the divalent cations and monovalent cations (except Li^+) during the late ion-intercalation process. The variation of the crystal structure of $Ti_3C_2T_z$ during the electrochemical process is explored by in situ X-ray diffraction (XRD).

2. Results and Discussion

The scanning electron images show that $Ti_3C_2T_z$ has common accordion-like multilayers of MXene (Figure S1A,B, Supporting Information), implying a successful exfoliation. The MXene-carbon nanotube ($Ti_3C_2T_z$-CNT) electrode also shows the same morphology as the $Ti_3C_2T_z$ powder except that CNTs are distributed on the surface of $Ti_3C_2T_z$ particle (Figure S2, Supporting Information). CNTs entangle the MXene flakes and enhance the electrode's mechanical stability to avoid MXene loss during the desalination experiments. The removal of aluminum from the parent Ti_3AlC_2 MAX phase is confirmed by energy-dispersive X-ray (EDX) spectra of $Ti_3C_2T_z$ (Figure S3, Supporting Information). The XRD patterns (Figure S1C, Supporting Information) also confirm the presence of $Ti_3C_2T_z$-type MXene with repeating (00l) diffraction peaks. The (002) reflection of $Ti_3C_2T_z$ splits into two peaks (Figure S1D, Supporting Information), at 6.9° 2θ (d-spacing, 1.28 nm) and 8.2° 2θ (d-spacing, 1.08 nm). After heating at 80 °C under vacuum overnight, only one peak is seen at 8.5° 2θ (d-spacing, 1.04 nm), indicating that the split (002) peak is caused by the residual water in between the layers. Compared with the powder sample, the $Ti_3C_2T_z$ electrode shows almost the same (002) peak, demonstrating that the probe ultrasonication does not affect the inherent characteristics of $Ti_3C_2T_z$.

To investigate the ion selectivity of $Ti_3C_2T_z$ electrodes, we used a low concentration aqueous electrolyte of Li^+, Na^+, K^+, Ca^{2+}, and Mg^{2+}, with a concentration of 10 nM for each cation; and each charging and discharging process of 3 h. As shown in Figure S4 in the Supporting Information, the potential holding

of the $Ti_3C_2T_z$ remains below 0 V versus Ag/AgCl, ensuring that the $Ti_3C_2T_z$ electrode only uptakes cations.[24] **Figure 1** shows the cation concentration changes over time in the 2nd, 6th, 10th, and 17th cycles obtained by subtracting the baseline from the initial concentration curve. The 14th cycle is shown in Figure S5 in the Supporting Information. The baseline of each cycle is established by connecting the start and endpoint of each half-cycle (Figure S6, Supporting Information). During the charging process, in the beginning, the concentration of all the cations decreases over time. Moreover, the concentration changes of these five cations reach the maximum simultaneously, meaning that the intercalation of these cations is synchronous. This phenomenon is different from obvious dynamics-dependent electrosorption (e.g., monovalent cations are up-taken faster than divalent cations) in subnanometer pores of carbon materials.[8] The difference is attributed to the flexible interlayer spacing of $Ti_3C_2T_z$, which will increase (breathe) as the cations intercalate into $Ti_3C_2T_z$.[25] The maximum concentration change during the charging process follows $K^+ > Na^+ > Ca^{2+} \approx Mg^{2+} > Li^+$, implying that K^+ is preferred during this process. After around 50 min, the concentration change of monovalent cations is positive, while that of divalent cations is still negative. This phenomenon can be explained by ion exchange between monovalent and divalent cations, which is because Mg^{2+} and Ca^{2+} carry twice the amount of the charge as Li^+, Na^+, and K^+.[26]

Having a certain amount of negative electric charge applied to the MXene electrode, the required number of divalent cations would be less than (half) that of monovalent cations to compensate the same electric charge. Therefore, divalent cations have higher competitiveness for intercalation in a confined space between $Ti_3C_2T_z$ layers. A similar ion exchange between monovalent and divalent cations is also observed in the case of porous carbon electrodes, where ions are stored based on electrical double layers (EDLs). In EDLs, as long as the dilute-theory works, in the beginning, the majority of ions in the solution are preferred while subsequently they will be replaced by ions with higher valence.[27] After the 10th cycle, the cation exchange between divalent and Li^+ is very weak, concluded from no net concentration increase in the course of charging.

Figure 2 shows ion uptake capacities (calculated according to Equation (1)) versus charging time in different cycles. In the 2nd cycle (Figure 2A), before around 64 min, the Li^+, Na^+, and K^+ ion removal capacities steadily increase, representing the continuous uptake of these three cations. The maximum removal capacities are 0.041 mmol g^{-1} for Li^+, 0.083 mmol g^{-1} for Na^+, and 0.095 mmol g^{-1} for K^+. The removal capacities decrease from 64 to 180 min, caused by the ion exchange between monovalent and divalent cations. In contrast to the behavior of monovalent cations, Mg^{2+} and Ca^{2+} removal capacities constantly increase before reaching a plateau, with the maximum capacity of 0.12 and 0.086 mmol g^{-1}, respectively. The selectivity factors, M^{x+}/Li^+ (M = Na^+, K^+, Ca^{2+}, and Mg^{2+}), are calculated every 10 min (according to Equation (2)), illustrating the selectivity behavior of $Ti_3C_2T_z$ at different charging times (Figure 2A). From the studied ions, Li^+ is least preferred by $Ti_3C_2T_z$. Before 90 min of charging, $Ti_3C_2T_z$ preferably uptakes K^+ with a maximum selectivity factor of 2.5 (at 30 min), which will be interpreted by the intercalation process of the cations later herein. After 90 min, Mg^{2+} dominates and reaches the
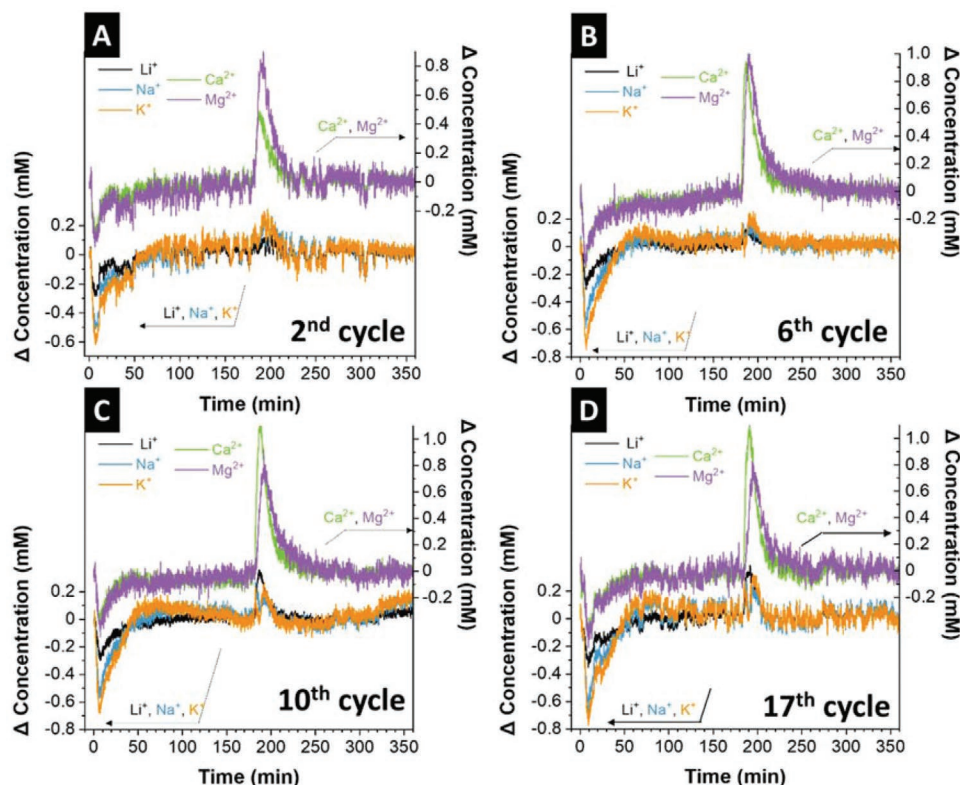
Figure 1. The concentration changes of Li^+, Na^+, K^+, Ca^{2+}, and Mg^{2+} during the A) 2nd, B) 6th, C) 10th, and D) 17th cycle with a flow rate of 1.1 mL min^{-1}.

highest selectivity factor of 3.9 at 180 min, attributed to the ion exchange between monovalent and divalent cations.

To investigate the material structural changes during the electrochemical process, we conducted in situ XRD measurements. This was done in a coin cell instead of the desalination flow cell while using the same electrolyte and same mass ratio between cathode and anode. The (002) peak shift is illustrated for five X-ray diffractograms for each charging/discharging process (Figure S7, Supporting Information). Without an external circuit, the intercalation distance (the distance between two Ti atoms) is about 0.57 nm (without considering any surface functional groups), calculated by subtracting the theoretical thickness of the MX-layer (Ti-C-Ti-C-Ti)[28] from the d-spacing obtained from XRD measurement (Figure S8, Supporting Information). This value is slightly larger than that of the pristine $Ti_3C_2T_z$ electrode (0.51 nm). The intercalation distance of the electrode soaked in deionized water (0.51 nm) suggests that the water and cations cannot spontaneously co-intercalate into the hydrofluoric acid (HF)-etched $Ti_3C_2T_z$, in agreement with the previous study.[29] After charging, the (002) reflection shifts to 5.78° 2θ, corresponding to a d-spacing of 1.53 nm, that is, 1.05 nm of intercalation distance (Figure 4A). Considering that the initial intercalation distance is less than the smallest hydrated diameters of these five cations in the bulk water (K^+, 0.662 nm; Figure S9, Supporting Information), all cations must (partially) dehydrate to intercalate into the $Ti_3C_2T_z$ layers. The dehydration energy (normalized by the charge) of K^+ is the lowest while that of Li^+ is the highest.[22] As a result, K^+ is

most preferred, whereas Li^+ is least preferred in the beginning. However, in the late charging stages, Mg^{2+} is most preferred instead of K^+, and Ca^{2+} becomes the second preferred cation (**Figure 3**A) due to the ion exchange effect.

The other cycles resemble the 2nd cycle and the difference lies only in the slightly different magnitude of removal capacities (Figure 2B–D; Figure S5B, Supporting Information). However, selectivity factors exhibit different trends from the 10th cycle. In the 2nd and 6th cycle, the selectivity factors of K^+/Li^+ and Na^+/Li^+ decrease gradually over time (Figure 3A,B), while from the 10th cycle, they drop steeply from 50 min (charging time); and at the end of the charging period, the amount of removed Na^+ and K^+ ions is less than that of Li^+ (Figure 3C,D and Figure S5C, Supporting Information). For example, the selectivity factors of K^+/Li^+ and Na^+/Li^+ at 180 min in the 14th cycle are 0.7 and 0.5, respectively. This indicates that Li^+ barely participates in the ion exchange after the 10th cycle. Additionally, the maximal selectivity factors of Na^+, K^+, Ca^{2+}, and Mg^{2+} all decrease from the 6th cycle to the 17th cycle. This may be due to the growth of amorphous TiO_2 on the surface of $Ti_3C_2T_z$ (Figure S10, Supporting Information), which has a lower Li diffusion barrier.[30]

In situ XRD (**Figure 4**) indicates that from the 10th cycle, one more (002) reflection appears at about 6.5° 2θ (d-spacing, ≈1.34 nm) apart from that initially at ≈5.8° 2θ (corresponding to a d-spacing of 1.53 nm). In the 6th cycle, (002) at 6.5° 2θ already appears with low intensity and broad shape. Among the two latter layer spacings, 1.53 nm is a value similar to the reported

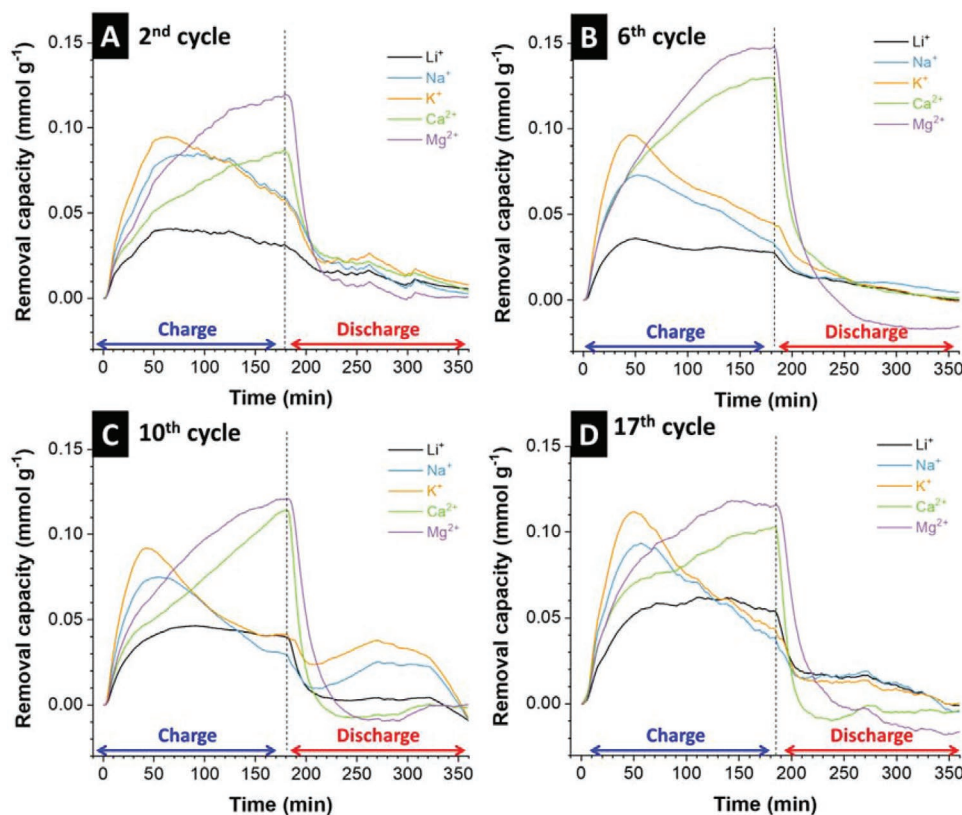**ADVANCED**
SCIENCE NEWS
www.advancedsciencenews.com

ADVANCED
SUSTAINABLE
SYSTEMS
www.advsustainsys.com

Figure 2. The ion removal capacity of Li$^+$, Na$^+$, K$^+$, Ca^{2+}, and Mg^{2+} during the A) 2nd, B) 6th, C) 10th, and D) 17th cycle with a flow rate of 1.1 mL min^{-1}.

results of kosmotropic cations (Li$^+$, Na$^+$, Mg^{2+}, and Ca^{2+}) intercalated Ti$_3$C$_2$T$_z$ at high relative humidity. In comparison, 1.34 nm is a value close to chaotropic cations found for K$^+$-intercalated Ti$_3$C$_2$T$_z$ at high relative humidity.[29] This indicates that the kosmotropic cations dictate the *d*-spacing of Ti$_3$C$_2$T$_z$ in the 2nd cycle. The second reflection, occurring after the 10th cycle, may result from partially desolvated, kosmotropic cations intercalating Ti$_3$C$_2$T$_z$.[31] This may relate to changes in the surface functional groups. In addition, during charging, the reflection shifts toward larger diffraction angles. The associated shrinkage of the *d*-spacing may be related to decreased electrostatic repulsions between negatively charged Ti$_3$C$_2$T$_z$ sheets due to cation intercalation.[32] During discharging, the Ti$_3$C$_2$T$_z$ sheets expand. While shrinking lasts over the whole charging process (180 min), the expansion is observed only for about an initial 45 min into the discharge process. This can be explained by continued cation intercalation during the whole charging time, caused by the ion exchange. Whereas, there is almost no cation deintercalation after about 45 min during the discharging process (Figure 4B–E).

We additionally studied the selective behavior of Ti$_3$C$_2$T$_z$ at a higher flow rate of feed water. In case of a flow rate double as much as before, the ion exchange phenomenon still occurs. However, before the ion exchange occurs, the removal capacities of Ca^{2+} and Mg^{2+} are much higher (Figures S11 and S12, Supporting Information), signaling that the divalent cations are more preferred at a higher flow rate. This is because the higher flow rate reduces the residence time that each cation in the feed

water spends near the electrode surface. As a result, divalent ions, with a higher charge and diffusion rate in the electrolyte,[33] enter the electrodes more readily than monovalent ones.

Development of a selective separation system, such as the one introduced in the present study, is well in alignment with UN's Sustainable Development Goals (SDGs) on a number of different levels. Such a system can specifically remove undesired ions (for example, ions responsible for scaling/fouling such as Ca^{2+}) or recover valuable ions like Li$^+$ from industrial wastewater or seawater. Recovery of lithium, particularly, is of great economical interest for the decades to come, as it serves as a key element in construction of Li-ion batteries for electric vehicles and portable electronics. As such, we can envision that the findings presented in this work can contribute to SDGs number 2, 6, 9, and 11–15, encompassing: sustainable management of water and industrialization, sustainable consumption and production patterns, climate change mitigation, sustainable use of the oceans and terrestrial ecosystems, sustainable agriculture, and the development of sustainable cities and human settlements.

3. Conclusions

In summary, our work investigates the selectivity of Ti$_3$C$_2$T$_z$ toward common alkali and alkaline earth cations. By online monitoring via ICP, we find that the ion-selective behavior of Ti$_3$C$_2$T$_z$ depends on the charging time. In the early charging
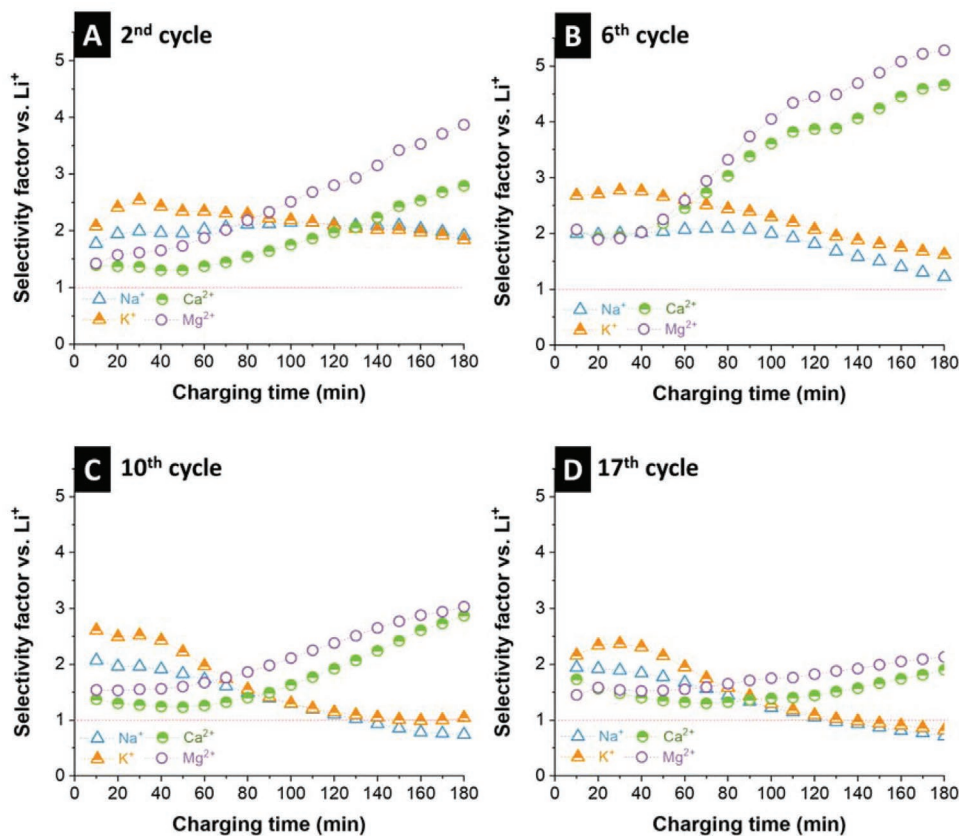
Figure 3. The selectivity factor versus Li^+ of Na^+, K^+, Ca^{2+}, and Mg^{2+} during the A) 2nd, B) 6th, C) 10th, and D) 17th cycle with a flow rate of 1.1 mL min^{-1}.

stages (before about 50 min), benefiting from the least dehydration energy, K^+ is preferred, with the maximum selectivity factor of 2.5 ± 0.2. Subsequently (70–90 min), due to the ion exchange effect between monovalent and divalent cations, the removal capacities of Ca^{2+} and Mg^{2+} (highest value about 0.12 mmol g^{-1}) increase and exceed that of K^+ at the end of charging time. Meanwhile, fewer Na^+ and K^+ compared with Li^+ are immobilized in $Ti_3C_2T_z$ (from the 10th cycle). In situ XRD data shows a symmetric (002) reflection of $Ti_3C_2T_z$ in the 2nd cycle. In contrast, after the 10th cycle, the asymmetry of the (002) reflection aligns with the emergence of two individual and overlapping peaks associated with the coexistence of cations with a different coordination number of water molecules. This could be an interesting preprocessing step for lithium recovery techniques. Meanwhile, we see potential to extend this approach to other MXene types and other ionic systems such as trivalent cations or metal-organic complexes.

4. Experimental Section

Materials and Material Synthesis: The parent Ti_3AlC_2 MAX phase was synthesized by mixing titanium (Ti, −325 mesh, 99%, Alfa Aesar), aluminum (Al, −325 mesh, 99.5%, Alfa Aesar), and graphite (C, 7–11 μm, 99%, Alfa Aesar) with atomic ratio of Ti:Al:C = 3:1.2:1.88 in a Turbula T2F mixer for 3 h using zirconia balls, followed by sintering inside a Sentro Tech induction furnace (STT-1700C-2.5-12, SN: 1052217) an alumina tube at 1600 °C for 2 h. A heating rate of 10 °C min^{-1} was used to reach the maximum temperature. After the holding time, the sample was left

to cool to room temperature. The sintering process was done under flowing argon.

To prepare $Ti_3C_2T_z$, Ti_3AlC_2 was ground to less than 45 μm and slowly added to 10 mass% aqueous HF (Acros Organics, 47–51 mass%). For each 1 g of MAX powder, 10 mL of the acidic solution was used. The mixture was stirred at 27 °C for 24 h. To remove HF and other unwanted products, the mixture was divided equally and distributed to 50 mL centrifuge tubes to have 0.5 g of MAX phase per tube. Deionized (DI) water was added to fill up the tubes to 50 mL. The tubes were centrifuged at 3500 rpm for 5 min to sediment the powders, the supernatant was discarded as hazardous waste. DI water was then added and the sediment was fully redispersed using a vortex machine. The washing step was repeated several times until a pH > 6 was obtained. At that point, the powders were collected and dried using vacuum-assisted filtration at room temperature overnight.

Electrode Preparation: Activated carbon (YP-80F, Kuraray) was mixed with polytetrafluoroethylene binder (60 mass% solution in water from Sigma-Aldrich) in 95:5 carbon: binder mass ratio. After adding ethanol, a sticky paste was obtained, which was subsequently cold-rolled (MTI HR01, MTI Corp.) to give 600 μm thick free-standing films and then dried in a vacuum oven at 120 °C overnight. These activated carbon film electrodes are labeled AC herein.

To fabricate MXene electrodes, $Ti_3C_2T_z$ was first mixed with multiwalled CNT (Graphene Supermarket) with a 90:10 MXene:CNT mass ratio. Then the mixture was stirred while being tip-sonicated in ethanol in an ice bath for 30 min using BRANSON Sonifier 450 (maximum power of 400 W) with 30% duty cycle and 30% power. The dispersed MXene-CNT in ethanol mixture was then vacuum filtered through polyvinylidene fluoride (PVDF) membranes (0.22 μm, Durapore), followed by excessive DI water filtration to remove residual salts or acids from the synthesis steps. The electrodes were then dried in a vacuum oven at 80 °C overnight.
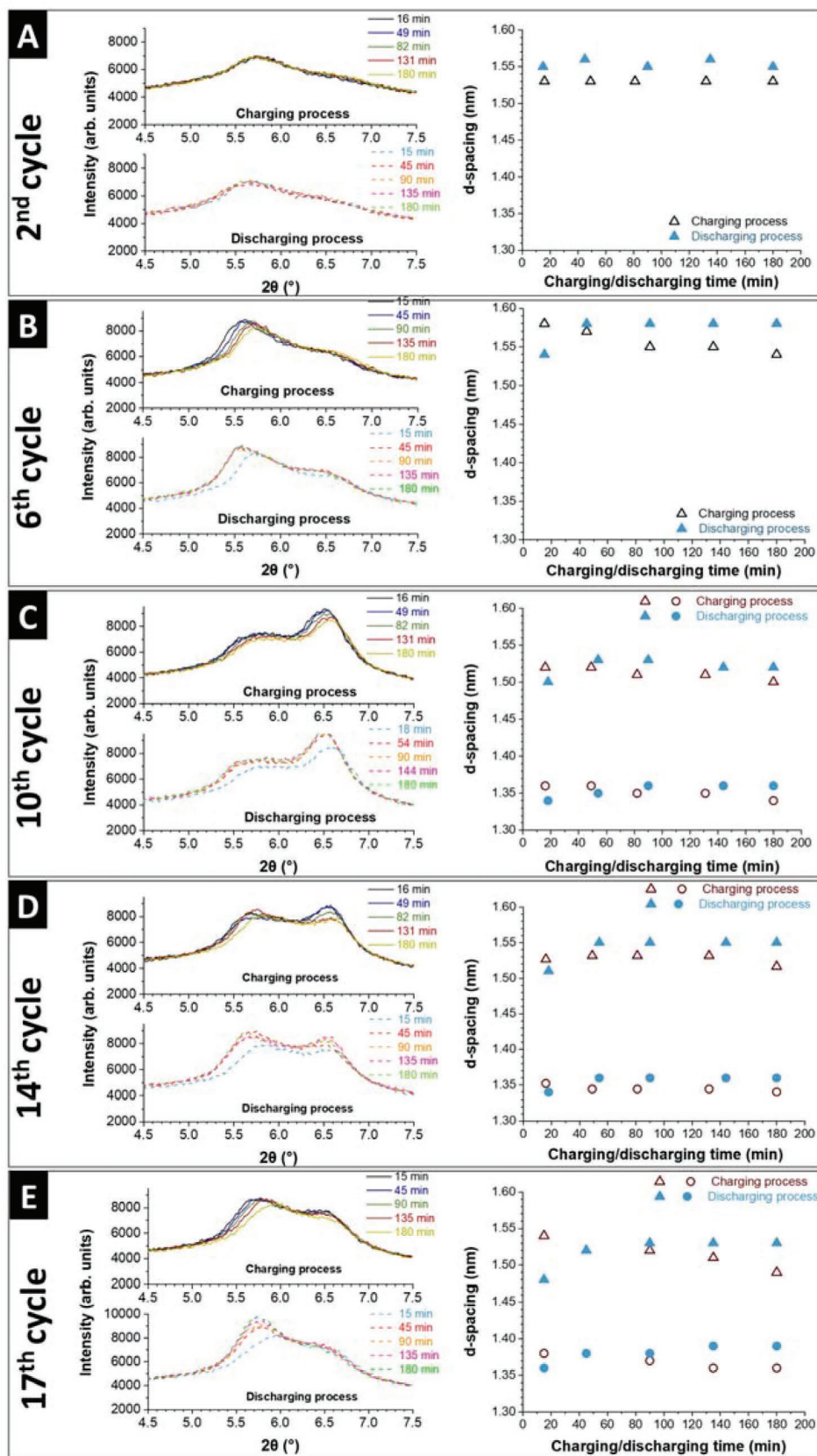
**ADVANCED
SCIENCE NEWS**

www.advancedsciencenews.com

**ADVANCED
SUSTAINABLE
SYSTEMS**

www.advsustainsys.com

Figure 4. In situ X-ray diffractograms from 4.5° 2θ to 7.5° 2θ of $Ti_3C_2T_z$ electrode and corresponding d-spacing, in different cycles: A) 2nd, B) 6th, C) 10th, D) 14th, and E) 17th cycle. Five X-ray diffractograms are shown for the charging/discharging process of each cycle.

**ADVANCED
SCIENCE NEWS**

www.advancedsciencenews.com

**ADVANCED
SUSTAINABLE
SYSTEMS**

www.advsustainsys.com

Electrochemical Ion Separation Experiments: The electrochemical ion separation experiments were performed in a single-pass channel cell. Following the vacuum filtration of $Ti_3C_2T_z$ material (with 10 mass% CNT), a 30 mm diameter electrode (around 120 mg mass loading, 17 mg cm^{-2}, on a 30 mm diameter PVDF support) was punched and used as the working electrode. As the counter electrode, free-standing AC films were used, whose mass was adjusted according to the MXene electrode, as described in the previous work.[24] Based on the half-cell cyclic voltammograms of the $Ti_3C_2T_z$ electrode (Figure S13, Supporting Information), $Ti_3C_2T_z$:AC mass ratio of 1:1.7 was maintained for all full-cell experiments throughout this study. The $Ti_3C_2T_z$ and AC electrodes were separated by a central water channel filled with a glass fiber mat (GF/A, Whatman). A Ag/AgCl reference electrode was used as a spectator to measure the potential of the electrodes individually.

To prepare the electrolyte, LiCl, NaCl, KCl, CaCl$_2$, and MgCl$_2$ salts (Sigma-Aldrich) were dissolved in DI water. A 10 L tank containing Li$^+$, Na$^+$, K$^+$, Ca^{2+}, and Mg^{2+} with 10 mM concentration for each cation was used as the electrolyte reservoir. The reservoir was constantly flushed with nitrogen gas throughout the experiment to remove the oxygen from the solution to prolong the life of $Ti_3C_2T_z$ electrode, as was done in the previous work.[24,33] Before the cell undergoes charging or discharging, the cell rested overnight to eliminate the influence of adsorption. The cell was charged and discharged with a constant specific current of 0.1 A g^{-1}. The upper voltage limit was set to 1.2 V, where the voltage was held for 3 h, and the lower voltage limit was 0.3 V, where the voltage was held for 3 h.

The cell was operated for 20 cycles; each cycle consists out of a charging and discharging process. The outlet of the middle water channel was connected to an ICP-OES (ARCOS FHX22, SPECTRO Analytical Instruments) through a peristaltic pump (at the flow rate of 1.1 mL min^{-1}), where the changes of the ions' concentration were recorded online. The extracted solution fed into the ICP-OES system was consumed by the measurement. The measured intensity of the ICP-OES signal was transformed into the concentration according to the calibrated intensity-concentration curves. Finally, the cation removal capacity (mmol g^{-1}) was calculated according to Equation (1), and selectivity factors for lithium were calculated following Equation (2).

$$\text{Removal capacity} \left(\text{mmol/g}_{electrode} \right) = \frac{v}{1000 \cdot m} \int \Delta c \, dt \qquad (1)$$

where v is the flow rate (mL min^{-1}), m is the mass of $Ti_3C_2T_z$ electrode, t is the selected time of the cation uptake step (min), and Δc is the concentration change of the cations (mM).

$$\text{Selectivity factor} = \frac{\text{Removal capacity of a certain cation}}{\text{Removal capacity of lithium ions}} \qquad (2)$$

Material Characterization: XRD analysis was conducted using a D8 Discover diffractometer (Bruker AXS) with a copper X-ray source (40 kV, 40 mA) and a 1D detector. Scanning electron microscopy (SEM) images were obtained using ZEISS (Gemini 500) at acceleration voltages of 1–3 kV. EDX spectroscopy was carried out at 15 kV with X-Max Silicon Detector from Oxford Instruments attached as a column to the SEM instrument. The EDX spectra were recorded and analyzed via AZtec software.

In Situ X-Ray Diffraction: In situ XRD measurements were carried out using a customized CR2032 coin cell with Kapton windows on STOE Stadi P diffractometer equipped with a Ga-jet X-ray source (Ga-K_β radiation, $\lambda = 1.20793$ Å). The XRD patterns were collected in the transmission mode in the range of 2θ from 3.5° to 10.3°, with a step of 0.04° 2θ and 5 s per step with the equivalent counting time of around 15 min. A 13 mm diameter $Ti_3C_2T_z$ electrode with the mass loading of 8.5 mg cm^{-2} was used for the electrochemical testing to ensure the successful collection of the XRD diffraction signal. The mass ratio between $Ti_3C_2T_z$ electrode (cathode) and AC electrodes (anode) is also 1.7, the same as in the ICP experiments. The same charging and discharging processes as the above-mentioned electrochemical ion separation experiments were performed via potentiostat/galvanostat

(SP-150, BioLogic). The resulted patterns were converted based on the wavelength of Cu-K_α for easier comparison with the literature and ex situ XRD results.

Supporting Information

Supporting Information is available from the Wiley Online Library or from the author.

Conflict of Interest

The authors declare no conflict of interest.

Data Availability Statement

The data that support the findings of this study are available from the corresponding author upon reasonable request.

[1] S. Yang, F. Zhang, H. Ding, P. He, H. Zhou, *Joule* **2018**, *2*, 1648.
[2] H. Yoon, J. Lee, S. Kim, J. Yoon, *Sep. Purif. Technol.* **2019**, *215*, 190.
[3] L. Tian, W. Ma, M. Han, *Chem. Eng. J.* **2010**, *156*, 134.
[4] J. Zhou, Z. Jiao, Q. Zhu, Y. Li, L. Ge, L. Wu, Z. Yang, T. Xu, *J. Membr. Sci.* **2021**, *627*, 119246.
[5] J. Zhou, Y. Zhang, M. Balda, V. Presser, F.-D. Kopinke, A. Georgi, *Chem. Eng. J.*, https://doi.org/10.1016/j.cej.2021.133544.
[6] K.-J. Tan, X. Su, T. A. Hatton, *Adv. Funct. Mater.* **2020**, *30*, 1910363.
[7] F. Yu, L. Wang, Y. Wang, X. Shen, Y. Cheng, J. Ma, *J. Mater. Chem. A* **2019**, *7*, 15999.
[8] Y. Zhang, J. Peng, G. Feng, V. Presser, *Chem. Eng. J.* **2021**, *419*, 129438.
[9] P. Srimuk, X. Su, J. Yoon, D. Aurbach, V. Presser, *Nat. Rev. Mater.* **2020**, *5*, 517.
[10] C. Zhan, F. Aydin, E. Schwegler, A. Noy, T. A. Pham, *ACS Appl. Nano Mater.* **2020**, *3*, 9740.
[11] J. G. Gamaethiralalage, K. Singh, S. Sahin, J. Yoon, M. Elimelech, M. E. Suss, P. Liang, P. M. Biesheuvel, R. L. Zornitta, L. C. P. M. de Smet, *Energy Environ. Sci.* **2021**, *14*, 1095.

[12] P. Srimuk, J. Lee, S. Fleischmann, M. Aslan, C. Kim, V. Presser, *ChemSusChem* **2018**, *11*, 2091.

[13] S. Fleischmann, J. B. Mitchell, R. Wang, C. Zhan, D. E. Jiang, V. Presser, V. Augustyn, *Chem. Rev.* **2020**, *120*, 6738.

[14] C. Choi, D. S. Ashby, D. M. Butts, R. H. DeBlock, Q. Wei, J. Lau, B. Dunn, *Nat. Rev. Mater.* **2019**, *5*, 5.

[15] M. Naguib, V. N. Mochalin, M. W. Barsoum, Y. Gogotsi, *Adv. Mater.* **2014**, *26*, 992.

[16] P. Srimuk, J. Halim, J. Lee, Q. Tao, J. Rosen, V. Presser, *ACS Sustainable Chem. Eng.* **2018**, *6*, 3739.

[17] M. R. Lukatskaya, S. Kota, Z. Lin, M.-Q. Zhao, N. Shpigel, M. D. Levi, J. Halim, P.-L. Taberna, M. W. Barsoum, P. Simon, Y. Gogotsi, *Nat. Energy* **2017**, *2*, 17105.

[18] P. Srimuk, F. Kaasik, B. Krüner, A. Tolosa, S. Fleischmann, N. Jäckel, M. C. Tekeli, M. Aslan, M. E. Suss, V. Presser, *J. Mater. Chem. A* **2016**, *4*, 18265.

[19] X. Zhang, Z. Zhang, Z. Zhou, *J. Energy Chem.* **2018**, *27*, 73.

[20] I. Ihsanullah, *Chem. Eng. J.* **2020**, *388*, 124340.

[21] A. Sinha, Dhanjai, H. Zhao , Y. Huang, X. Lu, J. Chen, R. Jain, *TrAC, Trends Anal. Chem.* **2018**, *105*, 424.

[22] Q. Gao, W. Sun, P. Ilani-Kashkouli, A. Tselev, P. R. C. Kent, N. Kabengi, M. Naguib, M. Alhabeb, W.-Y. Tsai, A. P. Baddorf, J. Huang, S. Jesse, Y. Gogotsi, N. Balke, *Energy Environ. Sci.* **2020**, *13*, 2549.

[23] J. Sun, Q. Mu, T. Wang, J. Qi, C. Hu, *J. Colloid Interface Sci.* **2021**, *590*, 539.

[24] M. Torkamanzadeh, L. Wang, Y. Zhang, Ö. Budak, P. Srimuk, V. Presser, *ACS Appl. Mater. Interfaces* **2020**, *12*, 26013.

[25] J. Li, X. Yuan, C. Lin, Y. Yang, L. Xu, X. Du, J. Xie, J. Lin, J. Sun, *Adv. Energy Mater.* **2017**, *7*, 1602725.

[26] C.-H. Hou, P. Taboada-Serrano, S. Yiacoumi, C. Tsouris, *J. Chem. Phys.* **2008**, *129*, 224703.

[27] R. Zhao, M. van Soestbergen, H. H. M. Rijnaarts, A. van der Wal, M. Z. Bazant, P. M. Biesheuvel, *J. Colloid Interface Sci.* **2012**, *384*, 38.

[28] M. Shekhirev, C. E. Shuck, A. Sarycheva, Y. Gogotsi, *Prog. Mater. Sci.* **2021**, *120*, 100757.

[29] M. Ghidiu, J. Halim, S. Kota, D. Bish, Y. Gogotsi, M. W. Barsoum, *Chem. Mater.* **2016**, *28*, 3507.

[30] C. Liu, Y. Li, D. Lin, P.-C. Hsu, B. Liu, G. Yan, T. Wu, Y. Cui, S. Chu, *Joule* **2020**, *4*, 1459.

[31] E. S. Muckley, M. Naguib, H.-W. Wang, L. Vlcek, N. C. Osti, R. L. Sacci, X. Sang, R. R. Unocic, Y. Xie, M. Tyagi, E. Mamontov, K. L. Page, P. R. C. Kent, J. Nanda, I. N. Ivanov, *ACS Nano* **2017**, *11*, 11118.

[32] J. Come, J. M. Black, M. R. Lukatskaya, M. Naguib, M. Beidaghi, A. J. Rondinone, S. V. Kalinin, D. J. Wesolowski, Y. Gogotsi, N. Balke, *Nano Energy* **2015**, *17*, 27.

[33] L. Wang, K. Frisella, P. Srimuk, O. Janka, G. Kickelbick, V. Presser, *Sustainable Energy Fuels* **2021**, *5*, 3124.